CrossMark

Shape evolution of water and saline droplets during icing/melting cycles on superhydrophobic surface

Ehsan Rahimi, Ali Rafsanjani-Abbasi, Ali Davoodi*, Alireza Kiani-Rashid

Materials and Metallurgical Engineering Department, Faculty of Engineering, Ferdowsi University of Mashhad, Mashhad 91775-1111, Iran

A B S T R A C T

In this study, bright nickel coating and superhydrophobic nickel film with micro-nano cones were prepared by electrodeposition. The topography and morphology of films were characterized by SEM and AFM. The evolution of shape parameters of water droplet including contact angle and contact diameter were measured by successive icing/melting cycles at $-10/+25$ and relative humidity of $30 \pm 2\%$. In addition, the freezing delay time was measured as a function of the surface topography and morphology. In presence of micro-nano cones, longer freezing delay time (110 min) observed in comparison with bright nickel (34 min). Power spectral density of AFM images showed that the superhydrophobic film has higher roughness distribution in all frequencies than bright nickel film. Also, it was shown that saline droplet has similar contact angle with water droplet on superhydrophobic surface (slightly changes from $156 \pm 2°$ to $154 \pm 1.5°$) in ambient temperature. Furthermore, it was observed that contact angle of pure water and saline droplets was decreased in single icing/melting cycle to $141 \pm 2°$ and $138.6 \pm 1°$, respectively. The reason was attributed to formation of concave ice, capillary condensation and frosting. Finally, electrochemical measurements showed that after 40 icing/melting cycles (2 h icing at -20 °C and melting at 25 °C for each cycle) by immersing in pure water and saline solutions, corrosion resistance of the superhydrophobic nickel film presented fairly less protection level, particularly in saline solution.

1. Introduction

Adhesion and excessive accumulation of ice and snow on environmental equipment and structures are well known to cause serious problems in aircraft, telecommunication towers, ships, antennas, wind turbines, oil platforms, exposed pipe in atmosphere, refrigerator and etc. [1–4]. Each year, numerous failures due to ice accumulation are reported in Canada, Russia, Norway, Finland, Iceland and USA [5–8]. To counter this problems and performance improvement, various techniques that include melting and anti-icing processes have been developed [1,4,9,10].

The phenomenon which the water droplet bead up on the surface is called "Lotus effect" [11]. Inspired by this phenomenon, researchers have recently made significant progress in fabrication of superhydrophobic surfaces with a high contact angle (CA > 150°), low sliding angle (SA < 10°) and low contact angle hysteresis (CAH) [11–15]. These properties are important parameters for designing and manufacturing of anti-icing or icephobic and superhydrophobic surfaces [2,7,10,16–18].

The surface energy and texture, both play important role in adhesion strength and formation of frost on surfaces. Therefore, superhydrophobicity may be stated as a combination of surface chemistry (hydrophobicity) and structure (roughness) [7,8,16,19,20]. To explain the effect of surface roughness on hydrophobicity, Wenzel and Cassie/Baxter put forward their independent theories of Wenzel's and Cassie's state. According to Wenzel's theory, water droplets penetrate to the rough surface in contact mode and demonstrate low CA while in Cassie/Baxter model, a water droplet rest on the heterogeneous surface due to presence of air packets in grooves [21–23].

Superhydrophobic surfaces can be beneficial to prevent ice formation through condensation of water droplets and also they are able to lower adhesive strength between solid and water [16,20]. Recently, researchers demonstrated that with increase in freezing delay time, problems such as high adhesion strength and formation of frost will be lowered [1,7,24–27]. Indeed, freezing delay time is related to delay in the ice nucleation process and according to the classic theory of nucleation, this can be described by the kinetics of crossing the energy barrier between ice/water which cause water solidification [7,26]. Based on above explanations, surface energies seem to play a significant role in freezing delay time.
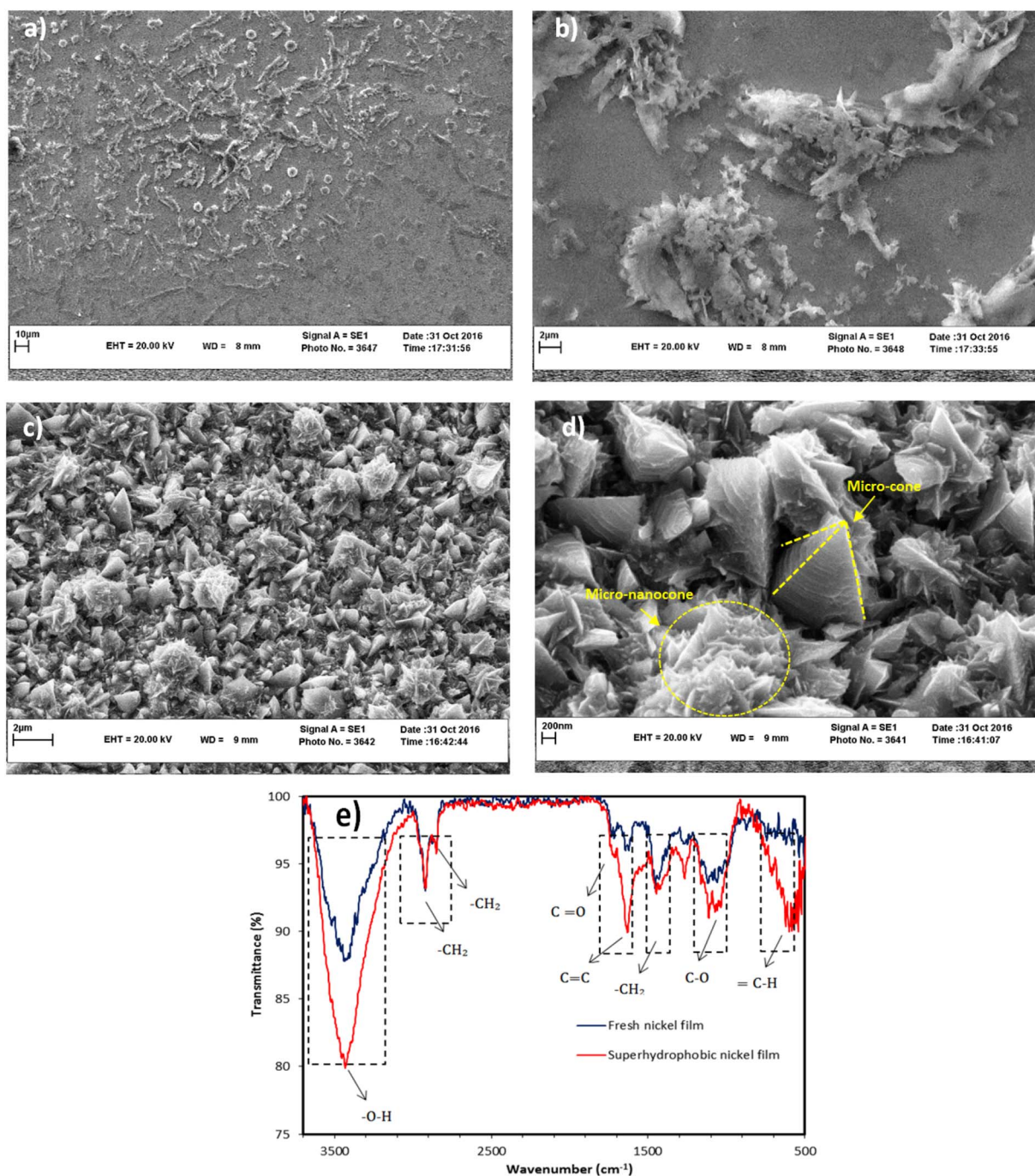
Fig. 1. SEM images of nickel surface fabricated by electro-deposition. (a, b) bright nickel film (c, d) the nickel MNCs, and (e) FT-IR spectra of nickel MNCs, black line: before exposing to air; red line: after exposing to air for 16 days. (For interpretation of the references to colour in this figure legend, the reader is referred to the web version of this article.)

Water is not pure in the nature and industrial areas and has some suspended and dissolved species such as dust and different salts [28–30]. In addition, icing/melting cycles have negative effects on the mechanical and corrosion properties of engineering structures near frozen saline soils in cold regions [29,31,32]. Wang et al. investigated the wettability of superhydrophobic copper surfaces; it was shown that the saline droplets have a high CA on copper surfaces [33]. Freezing point depression is a phenomenon where the freezing point of a solvent is decreased by the presence of salts. Also, it is noted that the lowering of freezing point does not depend on the nature of the solutes, rather only number of dissolved molecules and ions [29,31,34,35].

In this paper, we investigate the following items: A) effects of icing/melting cycles on shape parameters of water droplet on superhydrophobic nickel and bright nickel films and its correlation with surface roughness. B) Topography effects on freezing delay time. C) Water and saline droplets melting process and its effect on contact angle. D) Effect of icing/melting cycles by immersing in pure water and saline solution on corrosion behavior of superhydrophobic film.

2. Experiments and methods

2.1. Substrate material and surface treatment

A 99.5% nickel plate (40 mm × 40 mm × 1 mm) was employed as anode and nickel was deposited on the pure Cu plate as cathode (20 mm × 20 mm × 1 mm). The Cu plate was first ground through

successive grades of SiC paper to 3000 and polished with alumina paper. After that, the specimens were cleaned ultrasonically in acetone for 10 min, electro-polished at $20\ mA \cdot cm^{-2}$ in a solution containing $50\ g \cdot L^{-1} Na_2CO_3$ and $10\ g \cdot L^{-1}$ KOH for 1 min, activated in 10 wt% HCl at room temperature for 30 s and finally washed in deionized water.

2.2. Electrodeposition of nickel

Electrodeposition of nickel with micro-nano structure was conducted in the electroplating bath of 1 M $NiCl_2 \cdot 6H_2O$, 3.2 M H_3BO_3 and 0.9 M NH_4Cl. In order to obtain micro-nano film, the current density was $20\ mA \cdot cm^{-2}$ and $50\ mA \cdot cm^{-2}$ for 8 min and 1 min, respectively. The industrial bright nickel surface was also fabricated using another electroplating bath which was composed of 0.9 M $NiSO_4 \cdot 6H_2O$, 0.1 M $NiCl_2 \cdot 6H_2O$, 0.5 M H_3BO_3 and brightener agent at current density of $20\ mA \cdot cm^{-2}$ for 8 min. During deposition process, the temperature was kept at $60\ \pm\ 2\ ^{\circ}C$ for both baths. Also, coated surfaces were washed in deionized water and dried at ambient temperature at the end.

2.3. Characterization

The surface morphology of films was examined by scanning electron microscopy (SEM, Leo 1450 VP). Surface topography of micro-nano and bright nickel films were characterized by tapping mode of atomic force microscopy (AFM, NT-MDT Solver Next) which operated at scanning area of $20\ \mu m \times 20 \mu m$ and $5\ \mu m \times 5\ \mu m$ with a pixel resolution of 512×512 and scan frequency rate of 0.4 Hz. Surface chemical composition was analyzed using Fourier transformed infrared (FT-IR - AVATAR 370, Thermo Nicolet). The relative humidity (RH) inside freezing chamber was %30 $\pm$ 2 and freezing temperature for water and saline droplets was $-10\ \pm\ 1\ ^{\circ}C$ and $-20\ \pm\ 1\ ^{\circ}C$, respectively. For measuring CAH of superhydrophobic surface as a stickiness parameter, dynamic contact angle (DCA) was recorded. In addition, 7, 10 and 12 μl droplets were dropped on the surface during DCA measurement. The CA and CAH for different droplets are shown in Table S1 of Supporting information. In the following, 12 μl droplets of water and saline were placed carefully onto the surface of coated films for shape evolution observations. For measuring and analysis of CA and contact diameter (CD) of water and saline droplets, images captured by Canon SX 710 HS camera and processed by MATLAB and Image J (Drop Analysis LB-ADSA module) software.

Durability of superhydrophobic property was investigated under 40 icing/melting cycles by immersing in pure water and saline solution (2 h icing at $-20\ ^{\circ}C$ and melting at $25\ ^{\circ}C$ for each cycle). After this process, corrosion resistivity of superhydrophobic films were investigated by means of potentiodynamic polarization (PDP) and electrochemical impedance spectroscopy (EIS). The scan rate of PDP was $1\ mV \cdot s^{-1}$ and frequency range of EIS was 1 mHz to 30 kHz at ambient temperature. All electrochemical measurements were performed by Gill AC potentiostat (ACM instrument), using saturated calomel electrode (SCE, + 245 vs SHE) and a platinum foil as reference and counter electrode, respectively. The EIS equivalent circuit components are extracted using EIS spectrum analyzer software.

3. Results and discussion

3.1. Surface morphology and chemistry

The surface morphology of superhydrophobic and bright nickel films were observed by SEM. As shown in Fig. 1, bright nickel film (Fig. 1a, b) is relatively smooth and variations of surface roughness are negligible. On the other hand, the superhydrophobic sample in comparison with bright surface is fully covered with micro-nanocones (MNCs) with the mechanism of screw-dislocation driven (SDD) crystal growth which are prepared by two steps deposition process (Fig. 1c, d)

[36–38]. Based on the classical crystal growth theory for the supersaturation system, (SDD) growth occurs predominantly at low supersaturation [39]. In addition, supersaturation has direct correlation with driving force for crystal growth [36]. So, the driving force for crystal growth corresponds to the applied current density in electrodeposition. During electrodeposition of Ni ions on copper substrate, when current density adjusted on $20\ mA \cdot cm^{-2}$ for 8 min, system is in low supersaturation and lead to growth of micro cones with SDD crystal growth and increase of the film thickness. But with increasing the applied current density or high supersaturation ($50\ mA \cdot cm^{-2}$ for 1 min), new steps appear regardless of the location of screw dislocations (nanocones).

When the freshly prepared MNCs were exposed in air for 16 days, the CA was found to increase drastically from hydrophilic with CA of 10° to superhydrophobic with CA of 156° $\pm$ 2 and CD of 0.94 mm. The FT-IR spectra of fresh surface which is exposed to air are shown in Fig. 1e. Transition of superhydrophilicity to superhydrophobicity could be happened by adsorption of organic molecules (airborne organic hydrocarbons) on high surface energy sites which lead to reduce their surface free energy and reach to more stable condition. Absorption peaks such as $=C-H$ (600 cm^{-1}) and $-C\equiv C-$ (1634 cm^{-1}) are related to bending and stretching vibrations, respectively. Also, adsorption peaks at 1111, 1719 and 3432 cm^{-1} are evidences for presence of slight oxidation products or absorption of water from the environment. Another absorption peaks at 1450, 2847 and 2921 cm^{-1} depict the different vibration modes of C−H bonding which indicate the presence of the C−H group. By increasing intensity of the C−H and C−C bonds which act as hydrophobic region on the surface, surface free energy will decrease.

3.2. Effect of successive icing/melting cycles

The shape parameters evolution of water droplet on the superhydrophobic and bright nickel films are obtained by successive icing/melting cycles in $-10\ ^{\circ}C$ and $25\ ^{\circ}C$ and RH of 30 $\pm$ 2% (the superhydrophobic film with the droplet was placed into the cool freezing chamber). The macro-photograph images from different cycles of icing/melting cycles are shown in Fig. 2. Before the first cycle, the CA and CD are 156 $\pm$ 2° and 0.94 mm, respectively. For the accurate measurement of the freezing delay time, macro-photograph images with 2 minute intervals were taken from the water droplet on superhydrophobic surface in order to investigate the moment when droplet temperature reaches zero and the moment of droplet crystallization. Results showed that the droplet on superhydrophobic surface is still transparent after 106 $\pm$ 2 min and finally becomes non-transparent on superhydrophobic surface after 110 $\pm$ 2 min which indicates that it has frozen. After three successive icing/melting cycles, CA and CD were changed (see Fig. S1 of Supporting information) with freezing delay time of 110 min, 86 min and 70 min for first, second and third cycles, respectively. Also, Fig. 3 demonstrates that frost formation will increase along with successive icing/melting cycles.

The CA and CD of bright nickel film before freezing are 87.3 $\pm$ 2.2° and 1.7 mm, respectively. Before finishing the first cycle, the surface area fully covered by uniform frosts and no trace of the frozen drops can be seen (Fig. 3d). This change is due to presence of three phenomena during freezing process including: frost formation, drop evaporation process and the ice concave formation in contact with the drop [1,5,40]. When the superhydrophobic film is placed in $-10\ ^{\circ}C$ and RH of 30 $\pm$ 2%, frosts clearly can be seen on the surface after the first cycle which are due to moisture of environment (Fig. 3a). During the second cycle (Fig. 3b), upward freezing or accumulation of frosts on the surface can be observed [41,42]. These frosts (tiny condensed drops) as a result of the environmental temperature gradient, would first sit on the MNCs and then grow upwards which consequently decrease the wet contact with the solid surface. In the third cycle, it can be seen an increase of frost amount which cover the entire surface (Fig. 3c). By
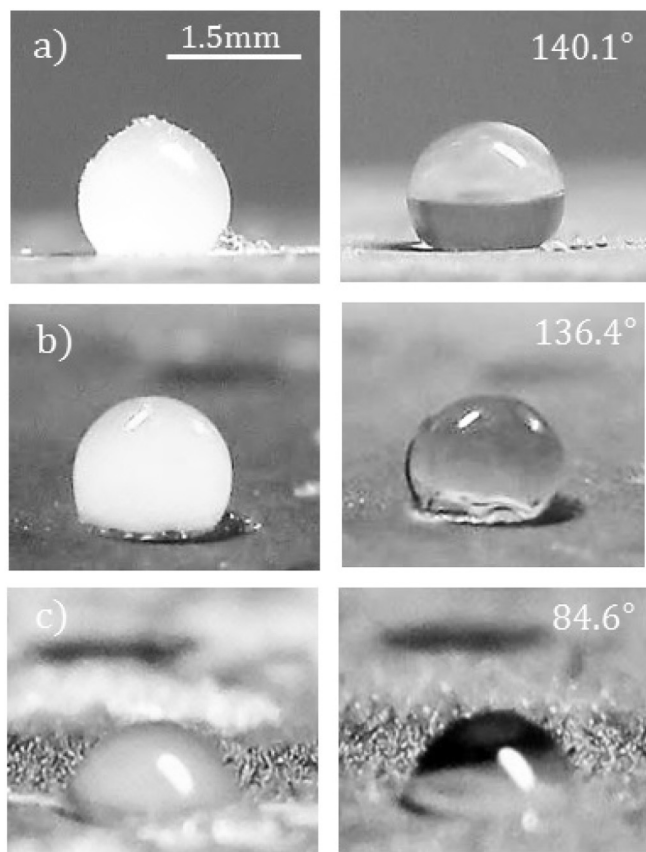
Fig. 2. Macro-photographs of shape parameters evolution of water droplet in successive icing/melting cycles on the superhydrophobic film for the first (a), second (b) and third (c) cycles.

passing time, the larger frosts will form near the water droplet which cause to reduce the CA. Another factor that affect the CA and CD is the presence of ice concave in contact with the water drop [7]. In each freezing cycle, ice concave increases due to capillary condensation, which is associated with an increase of CD. During freezing cycles, the droplet evaporation occurs as a result of vapor pressure difference between top of ice (low pressure region) and super cooled water (high pressure region) [1,5,40,42].

3.3. Surface topography

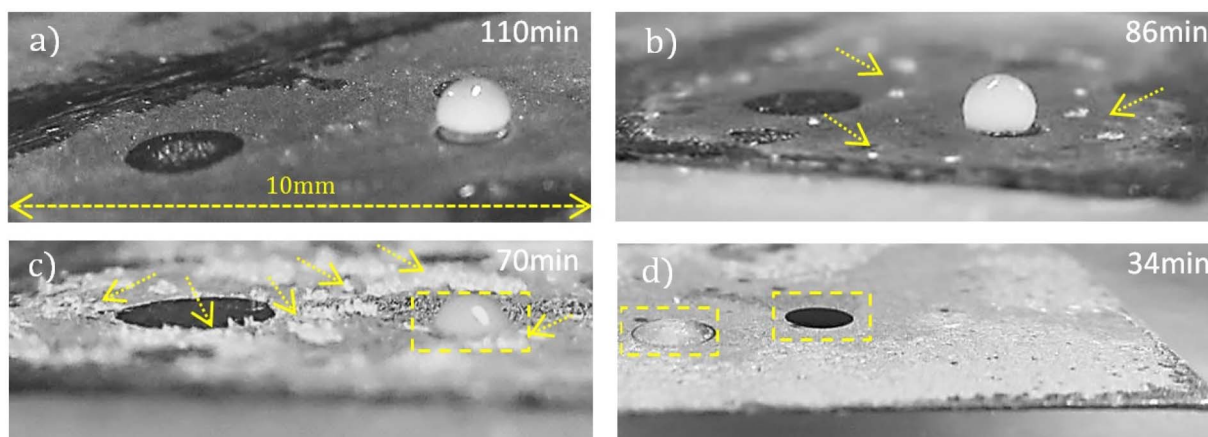Topographical features of surface have a critical effect on the wettability and hydrophobicity properties of coats and surfaces. In recent decades, many studies have been done in this field [43–47]. In this regard, AFM images from the bright and superhydrophobic nickel films in scanning area of $5\,\mu m \times 5\,\mu m$ and $20\,\mu m \times 20\,\mu m$ are shown in Fig. 4. The bright nickel sample has a low surface roughness, while the superhydrophobic sample has a high surface roughness caused by MNC structures. According to the height histogram in Fig. S2 of Supporting information, the value of surface roughness in bright nickel film with 2.1 nm root-mean-square (RMS) is very low as compared with the superhydrophobic film (RMS = 249.3 nm). The high average of height distribution in superhydrophobic film (600 nm) is a main reason for increasing the CA (regarding the presence of air packets in grooves of surface).

Fig. 5 shows the power spectral density (PSD) function, which provides the relative strength of roughness components as a function of spatial frequency. PSD can be calculated by Eq. (1) [38,43]:

$$PSD(f) = \lim_{A \to \infty} \frac{1}{A} \left| \int_A z(r) \exp(-2\pi i f \cdot r) dr \right|^2 \tag{1}$$

where z(r) represents the height data of the surface roughness, A is surface area of the measuring field, r is position vector and f is the spatial frequency vector in the $x - y$ plane. It can be seen in Fig. 5 that PSD function of superhydrophobic film shows higher spectral roughness than the bright nickel film at all spatial frequency regions. PSD of superhydrophobic film shows the uniformity at the entire frequencies that represents uniform distribution of nano cones and micro cones in high-frequencies and low-frequencies, respectively. However, the PSD of bright nickel film shows different slopes with height values between 64.2 nm and 156.4 nm, which indicate the uneven surface morphology. Furthermore, high roughness in superhydrophobic film is the basis of high CA and anti-frost characteristics. Therefore, the high surface roughness causes the accumulation of frosts (optically image in Fig. 3c) while for the bright film (optically image in Fig. 3d), lack of frosts accumulation can be seen clearly. These are critical factors that affect the freezing delay time which are discussed in next section.

3.4. Freezing delay time

Freezing delay time is one of the most important parameters in the field of icephobicity and anti-icing properties of materials [1,7,40]. The water droplet on superhydrophobic and bright nickel samples freezes after 110 min and 36 min at $-10\,°C$, respectively. This difference is due to surface roughness or surface topography and we know that the superhydrophobic surface could be explained with Cassie-Baxter theory [16,21–23]. When the superhydrophobic state changes from a Cassie-Baxter to Wenzel's state (metastable state), the CD would increase greatly because of electrostatic and van der Waals forces which enlarge
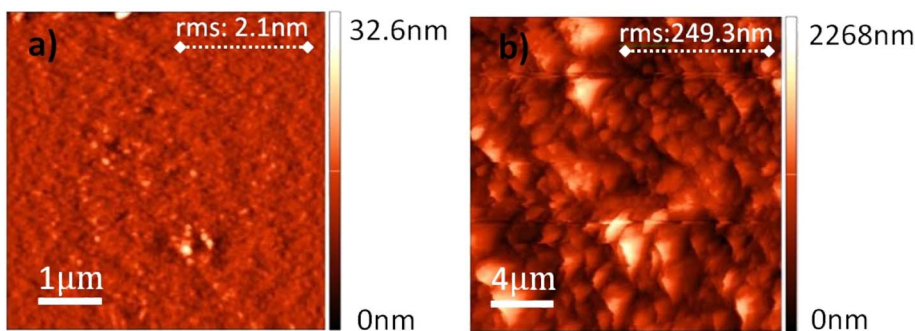

Fig. 3. The effect of successive icing/melting cycles on CA, CD and frost forming of (a, c) superhydrophobic film, and (d) single icing/melting cycle of bright nickel film.

Fig. 4. AFM images of (a) bright nickel film ($5 \times 5 \, \mu m^2$) and (b) superhydrophobic nickel film ($20 \times 20 \, \mu m^2$).
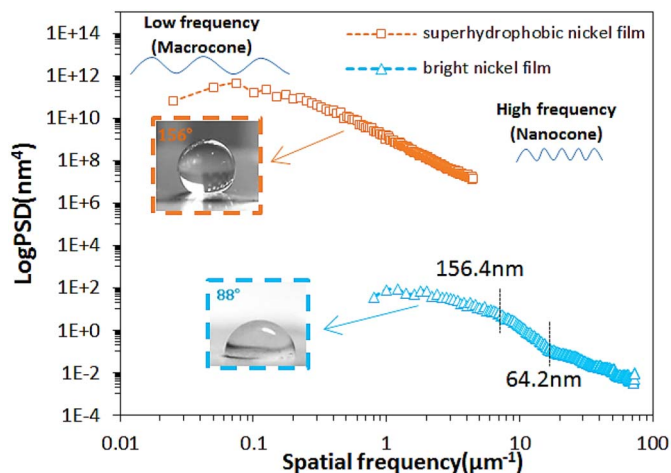

Fig. 5. Power spectral density (PSD) versus the spatial frequency for superhydrophobic and bright nickel films extracted from Fig. 4.

the solid/liquid adhesion [16,23].

The bright nickel surface increases the CD (solid/liquid contact) more than micro-nano structure since the water droplets condensed on the MNCs, have less contact with the solid surface. On the other hand, liquid has a more contact with the air packets which is an important factor in icephobicity properties [16]. Heat transfer processes between air/droplet/solid interfaces in micro-nano and smooth films which expose to open environment are schematically shown in Fig. 6. From the view point of thermodynamics, it is well known that when a drop exits on the surface, the droplet gains heat from the air in forms of heat conduction and thermal radiation. Also, it loses heat to the cold surface through the conduction and radiation between the drop and the MNCs. This relationship is expressed as [1]:

$$\Delta h = h_g + h_{g'} - h_l - h_{l'} \qquad (2)$$

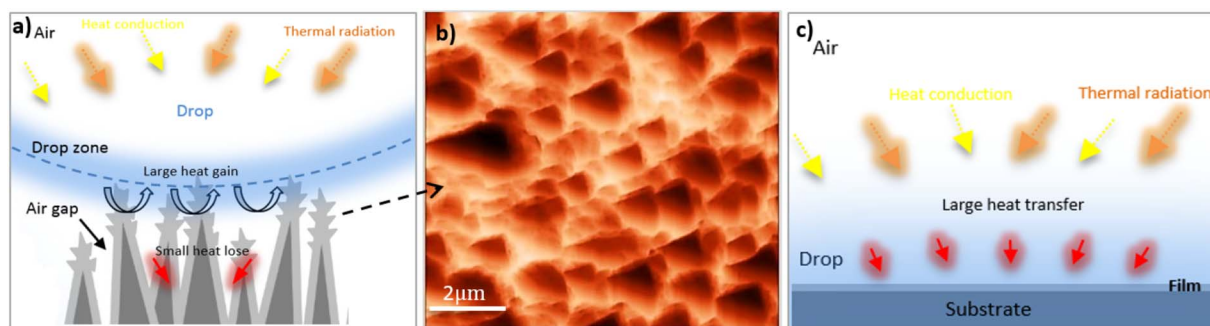where Δh is the net heat gain (unit time), h_g and $h_{g'}$ are heat gains

through heat transfer and thermal radiation (unit time), h_l and $h_{l'}$ are heat loss through heat transfer and thermal radiation (unit time). The decreased temperature in the drop (t_f) has an inverse relation with the net heat gain ($t_f \propto 1/\Delta h$) [1]. Consequently, with increasing Δh, t_f will reduce because of trapped air pockets through superhydrophobic structure and we have lower solid/liquid contact area during freezing procedure which leads to lower conduction heat transfer. As a result, higher Δh that means the lower contact in solid/liquid interface, reduces the heat loss of drops and maintains their temperature for more time.

3.5. Icing/melting cycle of water and saline droplet

The effect of single icing/melting cycle on CA and CD of the pure water ($-10\,°C$, RH 30%) and saline ($-20\,°C$, RH 30%) droplets which deposited on a superhydrophobic surface are shown in Fig. 7 by means of macro-photography. The CA and CD for water and saline droplets before freezing are 156°, 0.94 mm and 154°, 1.12 mm, respectively. Right after the freezing, the contact angle and drop height decrease for both droplets; Fig. 7c and i illustrates visual changes of ice droplets. These changes are caused by presence of frosts and metastable ice concaves around the frozen droplet. Metastable ice concaves are intrinsically related to release of the heat of crystallization during liquid to solid state transition which leads to enhancement of adhesion to a superhydrophobic surface [5,24,40].

Presence of local excess in the vapor pressure in comparison with the saturated values characteristic of the substrate temperature results in the desublimation of supersaturated vapors inside the gap between micro-nano structure and droplet and also the formation of frosts under the drop that leads to the transition from the heterogeneous to the mixed heterogeneous/homogeneous [5,48]. Therefore, growth of the ice concave is along with capillary condensation that clearly can be seen in Fig. 8a. As a result, increase in CD and decrease in CA are associated with the growth of the ice concave around frozen water droplet.

During the melting process of the water, accumulated frosts get

Fig. 6. Schematic side view of the heat transfer process in the open environment, (a) MNCs which have small heat transfer with water droplet, (b) AFM image of the superhydrophobic film ($10 \times 10 \, \mu m^2$) with black area of cones and golden light gaps which shows the conception of contact area and air packages in grooves, and (c) the smooth surface which has large heat transfer with water droplet.
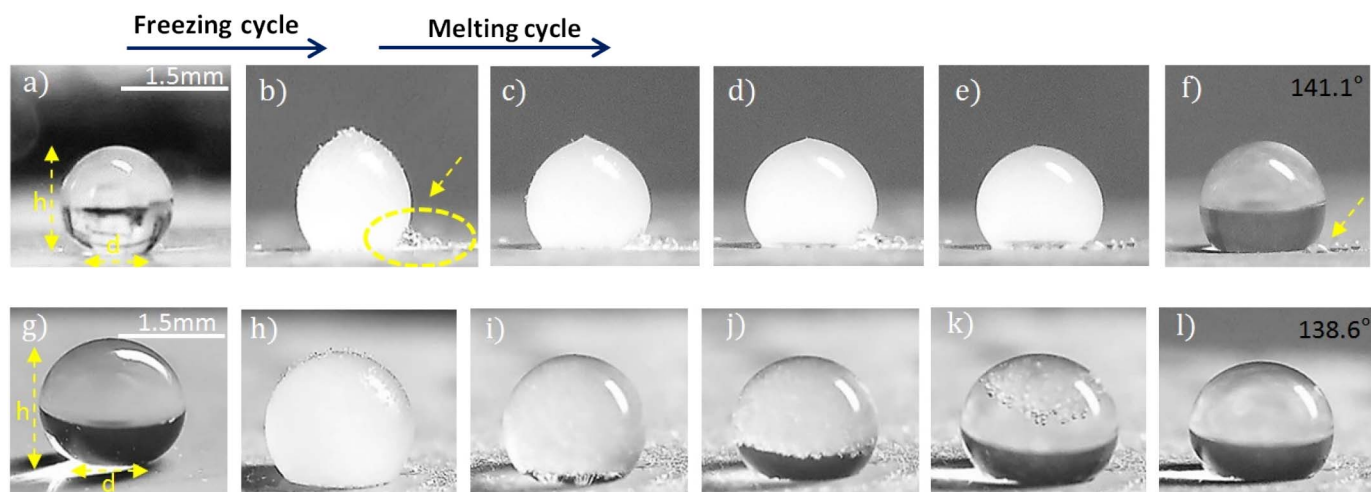
Fig. 7. Macro-photographs for the evolution of shape parameters during single icing/melting cycle for (a–f) water and (g–l) saline droplets on the superhydrophobic film.

away from the water droplet (tiny water droplets with hydrophobic state in Fig. 7f). Fig. 8 shows melting and deterioration process of ice concave in melting cycle of frozen water droplet while the saline droplet freezing mechanism is different than water droplet. Previous works show that the presence of impurities (salt and soil) on the surface causes to form a solution that is affect the CA and corrosion behavior [28,33]. In presence of soluble salts or solute molecules, the freezing point of the solution decreases because the vapor pressure of the saline solution is lower than pure water [5,26,35,49]. It is expected for saline solution that freezing point is decreased to c.a. − 2.2 °C [35,50,51]. However, once the solution starts freezing, it gets more and more concentrated. Therefore, the freezing point of concentrated part of the solution decreases to eutectic point of about 23.3 wt% of salt at − 21.1 °C in a manner that complete freezing has to take place with the formation of mixture of crystallohydrate ($NaCl \cdot 2H_2O$) and ice crystals. Consequently, as the saline (3.5 wt% NaCl solution) freezes, small ice crystals form in the pore spaces [35,51].

During saline droplet freezing, the diffusivity of Na^+ and Cl^- ions in the lattice are very low; as a result saline is isolated during freezing of ice and forms saline pockets [49]. Fig. 7i depicts that the saline droplet is slightly darker than the water droplet which is due to the concentrated saline packets and liquid-like films. The soluble salt may be moved by mass flow, concentration gradient and thermal gradient in the liquid film that is shown schematically in Fig. S3 (Supporting information) [28,49]. The melting process begins from metal surface due to temperature gradient between the frozen droplet and the surface. As a result, CA of water and saline droplets changes from superhydrophobic state to hydrophobic state. In this condition, the CA of water and saline droplets is 141° ± 2° and 138.6° ± 1.8, respectively.

3.6. Durability of superhydrophobic characteristic in icing/melting cycles

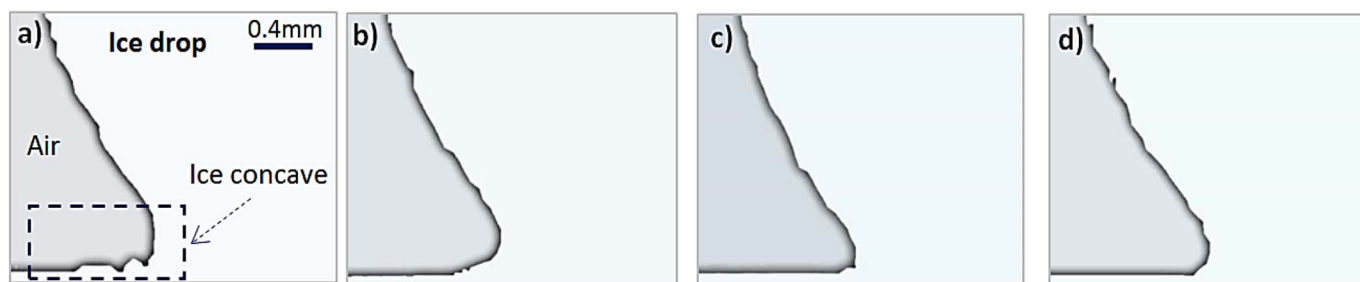Durability of superhydrophobic characteristic was investigated

using 40 icing/melting cycles (IMCs) by immersing in pure water and saline solutions by 2 h icing at − 20 °C and melting at 25 °C for each cycle. After 40 cycles, CA of water droplet on both superhydrophobic surfaces which were treated 40 IMCs in water and saline solutions decreased obviously. In this condition, the CA was 140° ± 1.6 and 129° ± 2 for pure water and saline solutions, respectively. Reduction of CA in two samples leads to increasing of contact area which has negative effects on superhydrophobicity, icephobicity and corrosion resistance. Therefore, electrochemical measurements were carried out to investigate the corrosion resistance of superhydrophobic surfaces after 40 icing/melting cycles.

Fresh superhydrophobic film and two films which are treated for 40 icing/melting cycles in pure water (IMCP) and saline (IMCS) were immersed in 3.5 wt% NaCl solution at 25 °C for potentiodynamic (PD) and electrochemical impedance spectroscopy (EIS) measurements. Corrosion current (i_{corr}) can be obtained by extrapolating of Tafel plots that are shown in Fig. 9 and corresponding data are listed in Table 1. According to Table 1, E_{corr} of superhydrophobic film is decreased for IMCP and IMCS while i_{corr} of superhydrophobic film is increased for IMCP and IMCS. These changes indicate that the IMCs damaged superhydrophobic structure due to mechanical stresses arising in three phase contact zone (solid/liquid/vapor) during crystallization of liquid and its melting [8,52]. The SEM images of IMCP and IMCS samples are presented in Fig. 10 which demonstrates the damages of MNCs.

IMCS sample is deteriorated more severely than IMCP due to presence of Cl^- ion in saline (Fig. 10b) but according to pervious works [7,10,27,53], the decrease in chemical stability of superhydrophobic film is critical factor in reducing the anti-icing and icephobicity properties of superhydrophobic surface. It has been investigated that the applied organic molecules could not provide dense enough surface layers, which allowed water molecules to reach the organic film/substrate interface and make the organic layer deteriorate gradually [10,52,53]. Boinovich et al. showed that the two different mechanisms
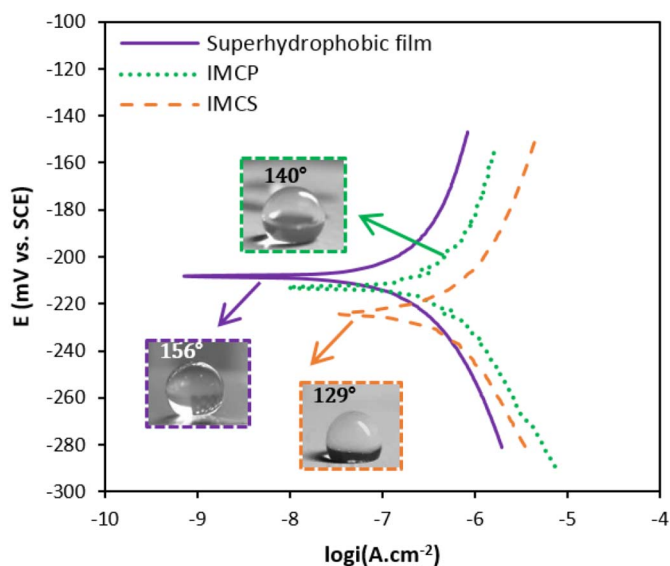

Fig. 8. Processed version of real images for ice concave evolution in melting cycle that is obtained from Fig. 7(b–e).

Fig. 9. Tafel measurements for superhydrophobic film before and after 40 icing/melting cycles by immersing in pure water (IMCP) and saline solution (IMCS) in 3.5 wt% NaCl aqueous solution at 25 °C.

Table 1
Corrosion data obtained from Tafel measurements.

Surface	i_{corr} (μA·cm^2)	E_{corr} (mV vs. SCE)	b_a (mV/decade)	b_c (mV/decade)
Superhydrophobic film	0.26	− 211.7	121.6	84.2
IMCP	0.54	− 213.2	63.2	45.4
IMCS	0.79	− 224.5	92.6	94.3

including the hydrolysis of free methylamine end groups with their substitution by hydroxyl end groups and the nonreversible hydration of hydrogen bonding active groups inside the hydrophobic and superhydrophobic material are responsible for deterioration of superhydrophobicity in long-term continuous contact of superhydrophobic surface with water [52]. As a result, these mechanisms along with mechanical stresses during crystallization of liquid and its melting, lead to the decrease in icephobicity property of superhydrophobic nickel surface during icing/melting cycles.

EIS is used to measure the dielectric properties of a medium and express them as functions of frequency [54–56]. EIS measurements were carried out at frequency range of 30 kHz to 10 mHz in 3.5 wt% NaCl solution that shown in Fig. 11. EIS results can be analyzed with the electrical equivalent circuit shown in Fig. 11b, which R_s represents solution resistance, R_{ct} the charge transfer resistance, R_f the resistance of the film (corrosion products), CPE_{dl} and CPE_f the constant phase elements of double-layer and corrosion film, respectively. The impedance of CPE is defined as [52,54]:

$$Z_{CPE} = \frac{1}{Y_0 (j\omega)^n} \tag{3}$$

where Y_0 is the modulus, j is imaginary unit, ω is the angular frequency, and n is the CPE exponent ($-1 \leq n \leq 1$) [56]. In general, in the Nyquist diagram (Fig. 11a) the interception of the real axis at higher frequencies is associated to the R_s and that which intercepts at the lower frequencies is attributed to R_{ct} which are an important parameters in the assessment of corrosion performance. It means that coatings with higher R_{ct} is expected to show higher corrosion resistance than lower values of it [54,56]. According to Table 2, R_{ct} of superhydrophobic film was decreased for IMCP and IMCS. Also, Fig. 11c shows the phase angle plots of superhydrophobic film, IMCP and IMCS with two time constants. The phase angle of the superhydrophobic film has decreased
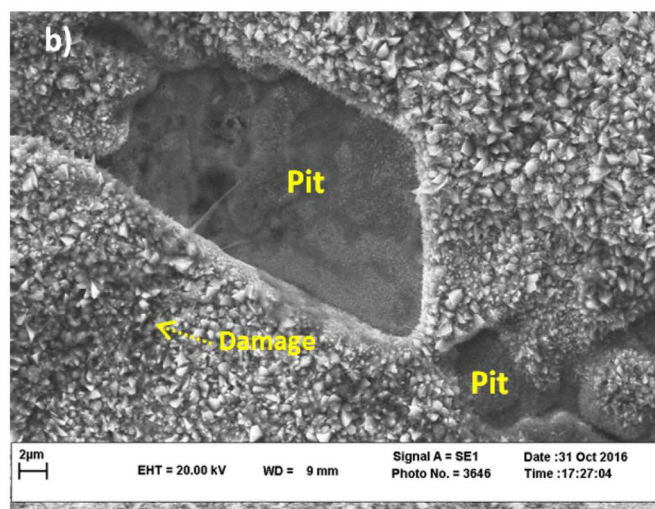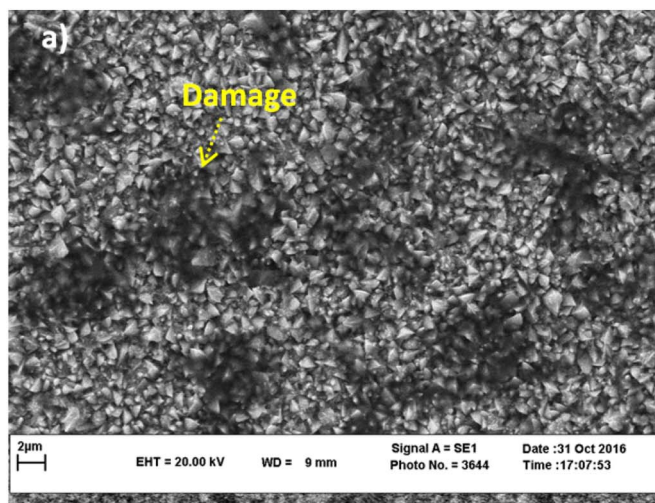

Fig. 10. SEM images of (a) IMCP and (b) IMCS.

after 40 cycles of icing/melting in water and saline solutions, which indicates that dielectric property of superhydrophobic film has decreased by deteriorating of morphology and hydrophobicity of the film [8].

4. Conclusions

The bright and superhydrophobic nickel films (micro-nanocones structure) were manufactured by electrodeposition method to analyze the shape parameter evolution of water and saline droplets during cyclic freezing and melting process. It was shown that surface morphology and topography of films play an important role in icephobicity/anti-icing of coats. Successive icing/melting cycles of water droplet on superhydrophobic film lead to decrease in contact angle and increase in contact diameter of droplet. This change in icephobicity performance is due to frost formation, drop evaporation process and ice concave formation in contact with the drop. The higher surface roughness will increase the freezing delay time compared with bright nickel film due to trapped air packets between water and micro-nanocones. Finally, in order to investigate the durability characteristic of superhydrophobic film, 40 icing/melting cycles by immersing in pure water and saline solution were performed. Results showed that the contact angle decreased for both samples, more enhanced in salt one, which is due to deterioration of morphology and formation of pitting
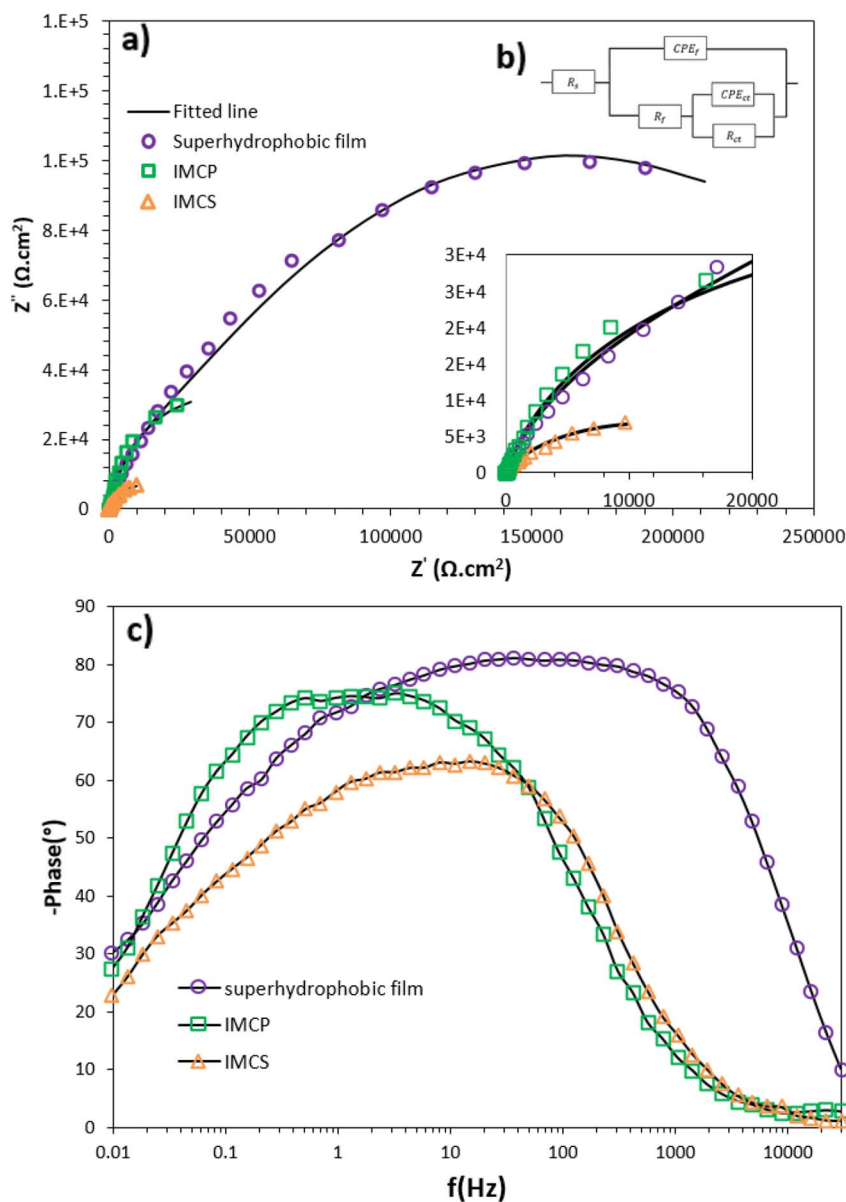
Fig. 11. EIS measurements for superhydrophobic film before and after 40 icing/melting cycles in pure water (IMCP) and saline solution (IMCS) in 3.5 wt% NaCl aqueous solution at 25 °C. (a) Nyquist plots, (b) electrical equivalent circuit, and (c) Bode phase plots.

Table 2
Corrosion data obtained from EIS measurements.

Surface	R_s ($\Omega \cdot cm^2$)	R_f ($k\Omega \cdot cm^2$)	CPE_f ($\mu F \cdot S^{-1} \cdot cm^{-2}$)	n_1	R_{ct} ($k\Omega \cdot cm^2$)	CPE_{ct} ($\mu F \cdot S^{-1} \cdot cm^{-2}$)	n_2
Superhydrophobic film	21.6	60.3	2.5	0.87	272.5	6.4	0.71
IMCP	61.2	6.5	34.8	0.88	73.6	5.3	0.91
IMCS	20.1	3.4	108.2	0.81	21.2	77.3	0.65

corrosion.

Acknowledgments

Supplementary data

Supplementary data to this article can be found online at https://doi.org/10.1016/j.surfcoat.2017.10.083.

References

[1] P. Guo, Y. Zheng, M. Wen, C. Song, Y. Lin, L. Jiang, Icephobic/anti-icing properties of micro/nanostructured surfaces, Adv. Mater. 24 (2012) 2642–2648.
[2] S. Farhadi, M. Farzaneh, S.A. Kulinich, Anti-icing performance of superhydrophobic surfaces, Appl. Surf. Sci. 257 (2011) 6264–6269.
[3] L.-O. Andersson, C.-G. Golander, S. Persson, Ice adhesion to rubber materials, J. Adhes. Sci. Technol. 8 (1994) 117–132.
[4] R. Menini, M. Farzaneh, Advanced icephobic coatings, J. Adhes. Sci. Technol. 25 (2011) 971–992.
[5] L.B. Boinovich, A.M. Emelyanenko, Role of water vapor desublimation in the adhesion of an iced droplet to a superhydrophobic surface, Langmuir 30 (2014) 12596–12601.
[6] S. Tarquini, C. Antonini, A. Amirfazli, M. Marengo, J. Palacios, Investigation of ice shedding properties of superhydrophobic coatings on helicopter blades, Cold Reg. Sci. Technol. 100 (2014) 50–58.

[7] S. Jung, M. Dorrestijn, D. Raps, A. Das, C.M. Megaridis, D. Poulikakos, Are super-hydrophobic surfaces best for icephobicity? Langmuir 27 (2011) 3059–3066.

[8] Y. Wang, J. Xue, Q. Wang, Q. Chen, J. Ding, Verification of icephobic/anti-icing properties of a superhydrophobic surface, ACS Appl. Mater. Interfaces 5 (2013) 3370–3381.

[9] C. Antonini, M. Innocenti, T. Horn, M. Marengo, A. Amirfazli, Understanding the effect of superhydrophobic coatings on energy reduction in anti-icing systems, Cold Reg. Sci. Technol. 67 (2011) 58–67.

[10] L.B. Boinovich, A.M. Emelyanenko, Anti-icing potential of superhydrophobic coatings, Mendeleev Commun. 23 (2013) 3–10.

[11] E. Celia, T. Darmanin, E. Taffin de Givenchy, S. Amigoni, F. Guittard, Recent advances in designing superhydrophobic surfaces, J. Colloid Interface Sci. 402 (2013) 1–18.

[12] A. Gupta, M.R. Joshi, N. Mahato, K. Balani, V. Verma, A. Agarwal, R. Narayan, Superhydrophobic surfaces, Biosurfaces: A Materials Science and Engineering Perspective, 2015, pp. 170–200.

[13] G. McHale, N. Shirtcliffe, M. Newton, Super-hydrophobic and super-wetting surfaces: analytical potential? Analyst 129 (2004) 284–287.

[14] L. Feng, S. Li, Y. Li, H. Li, L. Zhang, J. Zhai, Y. Song, B. Liu, L. Jiang, D. Zhu, Super-hydrophobic surfaces: from natural to artificial, Adv. Mater. 14 (2002) 1857–1860.

[15] L.B. Boinovich, A.M. Emelyanenko, A.S. Pashinin, C.H. Lee, J. Drelich, Y.K. Yap, Origins of thermodynamically stable superhydrophobicity of boron nitride nanotubes coatings, Langmuir 28 (2012) 1206–1216.

[16] M. Nosonovsky, V. Hejazi, Why superhydrophobic surfaces are not always icephobic, ACS Nano 6 (2012) 8488–8491.

[17] L. Cao, A.K. Jones, V.K. Sikka, J. Wu, D. Gao, Anti-icing superhydrophobic coatings, Langmuir 25 (2009) 12444–12448.

[18] S.A. Kulinich, M. Farzaneh, How wetting hysteresis influences ice adhesion strength on superhydrophobic surfaces, Langmuir 25 (2009) 8854–8856.

[19] C. Laforte, J. Laforte, J. Carrier, How a solid coating can reduce the adhesion of ice on a structure, Proceedings of the International Workshop on Atmospheric Icing of Structures (IWAIS), 2002.

[20] M. Susoff, K. Siegmann, C. Pfaffenroth, M. Hirayama, Evaluation of icephobic coatings—screening of different coatings and influence of roughness, Appl. Surf. Sci. 282 (2013) 870–879.

[21] R.N. Wenzel, Resistance of solid surfaces to wetting by water, Ind. Eng. Chem. 28 (1936) 988–994.

[22] A. Cassie, S. Baxter, Wettability of porous surfaces, Trans. Faraday Soc. 40 (1944) 546–551.

[23] R.J. Vrancken, H. Kusumaatmaja, K. Hermans, A.M. Prenen, O. Pierre-Louis, C.W.M. Bastiaansen, D.J. Broer, Fully reversible transition from Wenzel to Cassie − Baxter states on corrugated superhydrophobic surfaces, Langmuir 26 (2010) 3335–3341.

[24] P. Kim, T.-S. Wong, J. Alvarenga, M.J. Kreder, W.E. Adorno-Martinez, J. Aizenberg, Liquid-infused nanostructured surfaces with extreme anti-ice and anti-frost performance, ACS Nano 6 (2012) 6569–6577.

[25] A.J. Meuler, G.H. McKinley, R.E. Cohen, Exploiting topographical texture to impart icephobicity, ACS Nano 4 (2010) 7048–7052.

[26] L. Ickes, A. Welti, C. Hoose, U. Lohmann, Classical nucleation theory of homogeneous freezing of water: thermodynamic and kinetic parameters, Phys. Chem. Chem. Phys. 17 (2015) 5514–5537.

[27] M. Rahimi, A. Afshari, E. Thormann, Effect of aluminum substrate surface modification on wettability and freezing delay of water droplet at subzero temperatures, ACS Appl. Mater. Interfaces 8 (2016) 11147–11153.

[28] J.W. Cary, H.F. Mayland, Salt and water movement in unsaturated frozen soil1, Soil Sci. Soc. Am. J. 36 (1972) 549–555.

[29] K. Watanabe, T. Wake, Measurement of unfrozen water content and relative permittivity of frozen unsaturated soil using NMR and TDR, Cold Reg. Sci. Technol. 59 (2009) 34–41.

[30] P.M. Williams, M. Ahmad, B.S. Connolly, Freeze desalination: an assessment of an ice maker machine for desalting brines, Desalination 308 (2013) 219–224.

[31] Y. Lai, M. Liao, K. Hu, A constitutive model of frozen saline sandy soil based on energy dissipation theory, Int. J. Plast. 78 (2016) 84–113.

[32] X. Xu, Y. Wang, R. Bai, C. Fan, S. Hua, Comparative studies on mechanical behavior of frozen natural saline silty sand and frozen desalted silty sand, Cold Reg. Sci. Technol. 132 (2016) 81–88.

[33] P. Wang, D. Zhang, Z. Lu, Advantage of super-hydrophobic surface as a barrier against atmospheric corrosion induced by salt deliquescence, Corros. Sci. 90 (2015) 23–32.

[34] M. Fuchs, G.S. Campbell, R.I. Papendick, An analysis of sensible and latent heat flow in a partially frozen unsaturated soil1, Soil Sci. Soc. Am. J. 42 (1978) 379–385.

[35] J. Chang, J. Zuo, K.-J. Lu, T.-S. Chung, Freeze desalination of seawater using LNG cold energy, Water Res. 102 (2016) 282–293.

[36] F. Meng, S.A. Morin, A. Forticaux, S. Jin, Screw dislocation driven growth of nanomaterials, Acc. Chem. Res. 46 (2013) 1616–1626.

[37] Y. Deng, H. Ling, X. Feng, T. Hang, M. Li, Electrodeposition and characterization of copper nanocone structures, CrystEngComm 17 (2015) 868–876.

[38] E. Rahimi, A. Davoodi, A.R.K. Rashid, Characterization of screw dislocation-driven growth in nickel micro-nanostructure electrodeposition process by AFM, Mater. Lett. 210 (2018) 341–344.

[39] J.M. Lee, K.K. Jung, J.S. Ko, Formation of nickel microcones by using an electrodeposition solution containing H_3BO_3, Curr. Appl. Phys. 16 (2016) 261–266.

[40] J.B. Boreyko, B.R. Srijanto, T.D. Nguyen, C. Vega, M. Fuentes-Cabrera, C.P. Collier, Dynamic defrosting on nanostructured superhydrophobic surfaces, Langmuir 29 (2013) 9516–9524.

[41] E. Petit, E. Bonaccurso, General frost growth mechanism on solid substrates with different stiffness, Langmuir 30 (2014) 1160–1168.

[42] K. Rykaczewski, J. Chinn, M.L. Walker, J.H.J. Scott, A. Chinn, W. Jones, Dynamics of nanoparticle self-assembly into superhydrophobic liquid marbles during water condensation, ACS Nano 5 (2011) 9746–9754.

[43] M. Flemming, L. Coriand, A. Duparré, Ultra-hydrophobicity through stochastic surface roughness, J. Adhes. Sci. Technol. 23 (2009) 381–400.

[44] Y. Li, S. Dai, J. John, K.R. Carter, Superhydrophobic surfaces from hierarchically structured wrinkled polymers, ACS Appl. Mater. Interfaces 5 (2013) 11066–11073.

[45] Y. Gong, S.T. Misture, P. Gao, N.P. Mellott, Surface roughness measurements using power spectrum density analysis with enhanced spatial correlation length, J. Phys. Chem. C 120 (2016) 22358–22364.

[46] S. Singh, S. Basu, S.K. Ghosh, Structure and morphology of Cu/Ni film grown by electrodeposition method: a study of neutron reflectivity and AFM, Appl. Surf. Sci. 255 (2009) 5910–5916.

[47] N. Blondiaux, E. Scolan, A.M. Popa, J. Gavillet, R. Pugin, Fabrication of super-hydrophobic surfaces with controlled topography and chemistry, Appl. Surf. Sci. 256 (2009) S46–S53.

[48] K.K. Varanasi, T. Deng, J.D. Smith, M. Hsu, N. Bhate, Frost formation and ice adhesion on superhydrophobic surfaces, Appl. Phys. Lett. 97 (2010) 234102.

[49] R.C. Picu, V. Gupta, H.J. Frost, Crack nucleation mechanism in saline ice, J. Geophys. Res. Solid Earth 99 (1994) 11775–11786.

[50] D.G. Randall, J. Nathoo, A succinct review of the treatment of Reverse Osmosis brines using Freeze Crystallization, J. Water Process Eng. 8 (2015) 186–194.

[51] L.B. Boinovich, A.M. Emelyanenko, K.A. Emelyanenko, K.I. Maslakov, Anti-icing properties of a superhydrophobic surface in a salt environment: an unexpected increase in freezing delay times for weak brine droplets, Phys. Chem. Chem. Phys. 18 (2016) 3131–3136.

[52] L.B. Boinovich, A.M. Emelyanenko, A.S. Pashinin, Analysis of long-term durability of superhydrophobic properties under continuous contact with water, ACS Appl. Mater. Interfaces 2 (2010) 1754–1758.

[53] S.A. Kulinich, M. Honda, A. Zhu, A. Rozhin, X. Du, The icephobic performance of alkyl-grafted aluminum surfaces, Soft Matter 11 (2015) 856–861.

[54] K.-C. Chang, H.-I. Lu, C.-W. Peng, M.-C. Lai, S.-C. Hsu, M.-H. Hsu, Y.-K. Tsai, C.-H. Chang, W.-I. Hung, Y. Wei, J.-M. Yeh, Nanocasting technique to prepare lotus-leaf-like superhydrophobic electroactive polyimide as advanced anticorrosive coatings, ACS Appl. Mater. Interfaces 5 (2013) 1460–1467.

[55] A.C.C. de Leon, R.B. Pernites, R.C. Advincula, Superhydrophobic colloidally textured polythiophene film as superior anticorrosion coating, ACS Appl. Mater. Interfaces 4 (2012) 3169–3176.

[56] H.N. Shubha, T.V. Venkatesha, K. Vathsala, M.K. Pavitra, M.K. Punith Kumar, Preparation of self assembled sodium oleate monolayer on mild steel and its corrosion inhibition behavior in saline water, ACS Appl. Mater. Interfaces 5 (2013) 10738–10744.